Quantum Hall Conductance of Two-Terminal Graphene Devices

Quantum Hall conductance of two-terminal graphene devices

J. R. Williams,[1] D. A. Abanin,[2] L. DiCarlo,[3,*] L. S. Levitov,[2,4] and C. M. Marcus[3]

[1] *School of Engineering and Applied Sciences, Harvard University, Cambridge, MA 02138, USA*
[2] *Department of Physics, Massachusetts Institute of Technology, Cambridge, MA 02139, USA*
[3] *Department of Physics, Harvard University, Cambridge, MA 02138, USA*
[4] *Kavli Institute for Theoretical Physics, University of California, Santa Barbara, CA 93106*

(Dated: October 20, 2008)

Measurement and theory of the two-terminal conductance of monolayer and bilayer graphene in the quantum Hall regime are compared. We examine features of conductance as a function of gate voltage that allow monolayer, bilayer, and gapped samples to be distinguished, including N-shaped distortions of quantum Hall plateaus and conductance peaks and dips at the charge neutrality point. Generally good agreement is found between measurement and theory. Possible origins of discrepancies are discussed.

I. INTRODUCTION

Graphene monolayers and bilayers are recently discovered two-dimensional gapless semimetals. The Dirac spectrum of excitations in monolayer graphene gives rise to a number of novel transport properties, including anomalous quantized Hall conductance with plateaus at $4(n+1/2)\,e^2/h$, $n = 0, \pm1, \pm2, ...$ in multi-terminal samples.[1,2] Bilayer graphene has a quadratic, electron-hole-symmetric excitation spectrum, leading to quantized Hall conductance values $4n\,e^2/h$, $n = \pm1, \pm2, ...$[3,4] Both monolayer and bilayer graphene have a zeroth Landau level, located at the charge neutrality point (CNP), which is eightfold degenerate in bilayers and fourfold degenerate in monolayers. Other Landau levels are all fourfold degenerate in both types of graphene.[5,6] The novel transport signatures not only reflect this underlying band structure, but serve as an experimental tool for identifying the number of layers and characterizing sample quality.[4]

In recent work on graphene, two-terminal magnetoconductance has emerged as one of the main tools of sample characterization.[7,8,9] While a two-terminal measurement is not as straightforward to interpret as the corresponding multi-terminal measurement[10], it is the simplest to perform and may be the only measurement possible, for instance with very small samples. The presence of non-zero longitudinal conductivity causes quantum Hall plateaus measured in a two-terminal configuration to not be as well quantized as in multiprobe measurement.[4] As discussed in detail below, plateaus exhibit a characteristic N-shaped distortion arising from the finite longitudinal conductivity that depends on device geometry.

In this Article, we systematically examine two-terminal conductance in the QH regime for monolayer and bilayer graphene for a variety of sample aspect ratios (Table I). We especially focus on the features that can help to distinguish monolayer and bilayer graphene: the conductance extrema in the N-shaped distortions of the quantum Hall plateaus and at the CNP. We find that these features depend both on the sample aspect ratio and the number of graphene layers. Results are compared to recent theory[11], in which two-terminal conductance for arbitrary shape is characterized by a single parameter ξ, the effective device aspect ratio ($\xi = L/W$ for rectangular samples, where L is the length or distance between contacts, and W is the device width).

TABLE I: Measured two-terminal graphene devices.

Sample	Layers (Inferred)	$(L,\ W)$ [μm]	ξ_s	$\xi_{\rm fit}$
A1	Monolayer	(1.3, 1.8)	0.7	1.7
A2	Monolayer	(0.4, 2.0)	0.2	0.2
B1	Bilayer	(2.5, 1.0)	2.5	0.8
B2	Bilayer	(0.3, 1.8)	0.2	0.3
C	Monolayer	Asymmetric	0.9[a]	0.9

[a] effective aspect ratio, see Sect. IV.

In Ref. [11], the positions of conductance extrema on the distorted plateaus were linked to incompressible densities. Here we find that this relation can be used to distinguish monolayer and bilayer graphene devices even when the distortions of the plateaus are strong. The analysis of rectangular two-terminal samples is extended to a sample with asymmetric contacts, extracting an effective sample aspect ratio via conformal mapping. Best-fit values of the aspect ratio, $\xi_{\rm fit}$, obtained by fitting the theory to the experimental data, are compared to the measured sample aspect ratio, ξ_s. Agreement is generally good, but not uniformly so. We speculate on possible causes of these discrepancies, including inhomogeneous contact resistance, electron and hole puddles, and contributions of transport along p-n interfaces.

A. Qualitative Discussion

Representative theoretical plots of two-terminal conductance for monolayer, bilayer, and gapped bilayer graphene as a function of filling factor, ν, are shown in Fig. 1. For both monolayers and bilayers, the absence of an energy gap between the conduction and valence bands gives rise to a zero energy Landau level (LL)[5], which can

either increase or decrease the two-terminal conductance around the charge neutrality point, depending on the aspect ratio of the sample. The eightfold degeneracy of the zero-energy LL in bilayer graphene[6] enhances the size of this feature relative to monolayer graphene.

A gap in the spectrum of bilayer graphene opens when the on-site energy in one layer differs from the on-site energy in the other.[12] This may result, for instance, from asymmetric chemical doping[13] or electrostatic gating.[14] The gap splits the zero-energy LL, suppressing conductance at the CNP. The qualitative effect of a gap in the bilayer spectrum can be seen in Fig. 1 by comparing the gapped case [Fig. 1(c)], which always has a zero of conductance at $\nu = 0$, to the gapless cases [Figs. 1(a,b)], which has a non-zero value of conductance at $\nu = 0$.

Also illustrated in Fig. 1 is how the aspect ratio of the sample affects the two-terminal conductance near quantum Hall plateaus for all three spectrum types. Finite longitudinal conductivity leads to N-shaped distortions of the plateaus,[11] which are of opposite signs for aspect ratios $\xi < 1$ and $\xi > 1$. Note, however, that the extrema of conductance—minima for $\xi < 1$ and maxima for $\xi > 1$—are aligned with the plateaus centers, which coincide with the incompressible density values (different for monolayers and bilayers). Distorted plateaus thus remain useful for characterizing the number of layers and density.

The back-gate dependence of conductance for the five samples reported are most similar to those in Figs. 1(a,b), indicating that these samples are single layers and gapless bilayers only (see Table 1). We use the model of Ref. [11] to fit the conductance data treating the aspect ratio as a fit parameter. In doing so, our presumption is that the visible dimensions of the sample may not reflect the actual pattern of current flow. Since the conductance problem for a sample of any shape can be reduced to that of an effective rectangle via a conformal mapping[15,16,17], which depends on the sample shape but *not* on the conductivity tensor, the rectangular geometry is universal for two-terminal conductance. Thus the model of a conducting rectangle with an unspecified aspect ratio is suitable for describing systems in which current pattern is not precisely known.

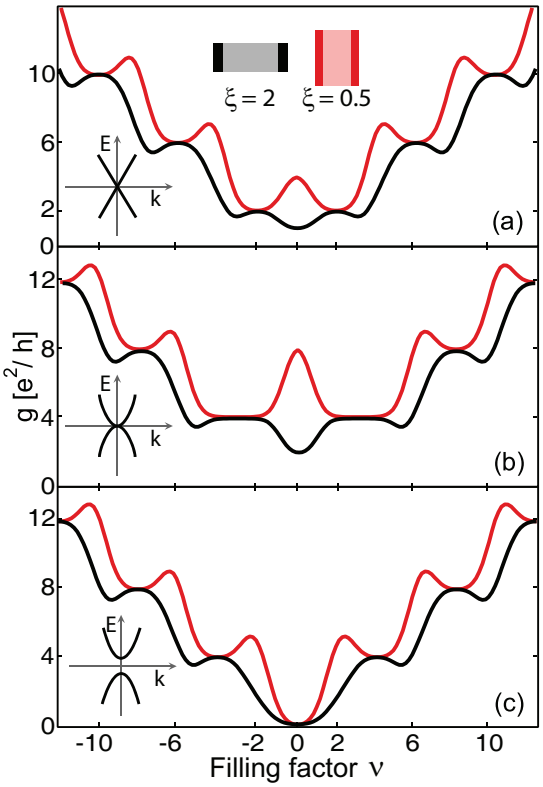

FIG. 1: (color online) Theoretical two-terminal QH conductance g as a function of filling factor ν (Ref. [11]) shown for (a) single-layer graphene (b) bilayer graphene (c) gapped bilayer graphene for effective aspect ratios $\xi = L/W = 2$ (black) and 0.5 (red). Finite longitudinal conductivity due to the states in the middle of each Landau level distorts the plateaus into N-shaped structures, which are of opposite sign for $\xi < 1$ and $\xi > 1$. Local extrema of g at filling factors $\nu = \pm 2, \pm 6, \pm 10...$ for single layers and at $\nu = \pm 4, \pm 8, \pm 12...$ for bilayers are either all maxima ($\xi < 1$) or all minima ($\xi > 1$). For gapless monolayer and bilayer samples (a,b), $g(\nu = 0)$ is a minimum for $\xi < 1$ and maximum for $\xi > 1$; for the gapped bilayer (c) g vanishes at $\nu = 0$ for all ξ.

B. Sample Fabrication and Measurement

Graphene devices were fabricated by mechanically exfoliating highly oriented pyrolytic graphite[18] onto a n^{++} Si wafer capped with $\sim 300\,\mathrm{nm}$ of SiO_2. Potential single and bilayer graphene flakes were identified by optical microscopy. Source and drain contacts, defined by electron beam lithography, were deposited by thermally evaporating 5/40 nm of Ti/Au. The aspect ratio, ξ_s, of each sample was measured using either optical or scanning electron microscopy.

Devices were measured in a ^{3}He refrigerator allowing dc transport measurements in a magnetic field $|B| < 8\,\mathrm{T}$ perpendicular to the graphene plane. Unless otherwise noted, all measurements were taken at base temperature, $T \sim 250\mathrm{mK}$. Differential conductance $g = dI/dV$, where I is the current and V the source-drain voltage, was measured using a current bias (I chosen to keep $eV < k_BT$) and standard lock-in technique at a frequency of 93Hz. All samples show $B = 0$ characteristics of high-quality single-layer and bilayer graphene[1,2]: a CNP positioned at back-gate voltage $V_{\mathrm{bg}} \sim 0$ and a large change in g (in excess of $20\,e^2/h$) over the V_{bg} range of $\pm 40\,\mathrm{V}$.

II. MONOLAYER SAMPLES

Figure 2(a) shows the two-terminal conductance $g(V_{\mathrm{bg}})$ for sample A1 ($\xi_s = 0.7$) at B= 8 T (black trace). Plateaus are seen at $\nu = \pm 2$ near—but not equal to—$2\,e^2/h$, with values of $\sim 2.3(2.7)\,e^2/h$ on the electron (hole) side of the CNP. At the CNP ($V_{\mathrm{bg}} \sim 2.3\mathrm{V}$), g departs from the quantized values, dropping to a mini-

mum of $\sim 1.4e^2/h$. At higher densities, the conductance exhibits a series of maxima with values slightly above 6, 10, $14\,e^2/h$. Maxima on the hole side consistently have slightly higher values, a feature observed in all the samples measured. The inset of Fig. 2(a) shows g in the QH regime as a function of $V_{\rm bg}$ and B. Dashed black lines indicate the filling factors $\nu = n_s h/eB$ (where n_s is the carrier density) of -6, -10, and -14 and lines align with the local *maxima* of $g(V_{\rm bg}, B)$. $V_{\rm bg}$ was converted to n_s using a parallel plate capacitance model[18], giving $n_s = \alpha(V_{\rm bg} + V_{\rm offset})$ with $\alpha = 6.7 \times 10^{10}{\rm cm}^{-2}{\rm V}^{-1}$ and $V_{\rm offset} = 2{\rm V}$.

Measured $g(V_{\rm bg})$ [black curve in Fig. 2(b)] for sample A2 ($\xi_s = 0.2$), made using the same graphene flake as A1, shows distinctive differences from the measured $g(V_{\rm bg})$ of sample A1. In particular, at the CNP ($V_{\rm bg} = -1.5{\rm V}$), g exhibits a sharp peak with a maximal value of $\sim 8.8\,e^2/h$. Away from the CNP, the conductance has maxima which are much stronger than those of sample A1. The inset of Fig. 2(b) shows $g(V_{\rm bg}, B)$. For this sample, the dashed lines representing the incompressible filling factors $\pm 6, \pm 10, \pm 14$ now align with the *minima* in g. Here we used the $V_{\rm bg}$ to n_s conversion factors of $\alpha = 6.7 \times 10^{10}{\rm cm}^{-2}{\rm V}^{-1}$ (the same as for sample A1) and $V_{\rm offset} = -1.1{\rm V}$.

The observed features in g for samples A1 and A2 can be compared to theory[11] for two-terminal quantum Hall conductance, which uses a model of a conducting rectangle $L \times W$ with a spatially uniform conductivity. The filling factor dependence of the conductivity tensor is obtained using the semicircle relation for quantum Hall systems, derived in Ref. [19], which is applied independently for each Landau level. Landau level broadening due to disorder is included in the theory as a gaussian broadening $e^{-\lambda(\nu-\nu_n)^2}$, where ν_n is the center of the LL and λ is a fitting parameter. The total conductivity tensor is taken to be a sum of the contributions of individual Landau levels. The current-density distribution for a rectangular sample with an arbitrary aspect ratio is found analytically by conformal mapping (see Refs. [15,16,17]). The current density is then integrated numerically along suitably chosen contours to evaluate total current and voltage drop, from which $g = I/V$ is obtained.

Along with the experimental traces, Figs. 2(a,b) also show the theoretical curves for the best-fit (solid red trace) and the actual sample aspect (dashed blue trace) ratios. For sample A1, the best-fit aspect ratio, $\xi_{\rm fit} = 1.7$, differs considerably from the measured value, $\xi_s = 0.7$. For sample A1, the best fit gives the Landau level broadening parameter $\lambda = 1.2$. This theoretical curve ($\xi_{\rm fit} = 1.7$) reproduces the essential features of the data: local maxima align with the filling factors $\pm 2, \pm 6, \pm 10$, ..., and g exhibits a dip at the CNP.

The alignment of conductance minima with densities corresponding to the integer filling factors as well as a peak at the CNP observed for sample A2 are consistent with theoretical predictions for a short, wide monolayer graphene sample. As illustrated in Fig. 2(b), the best-fit

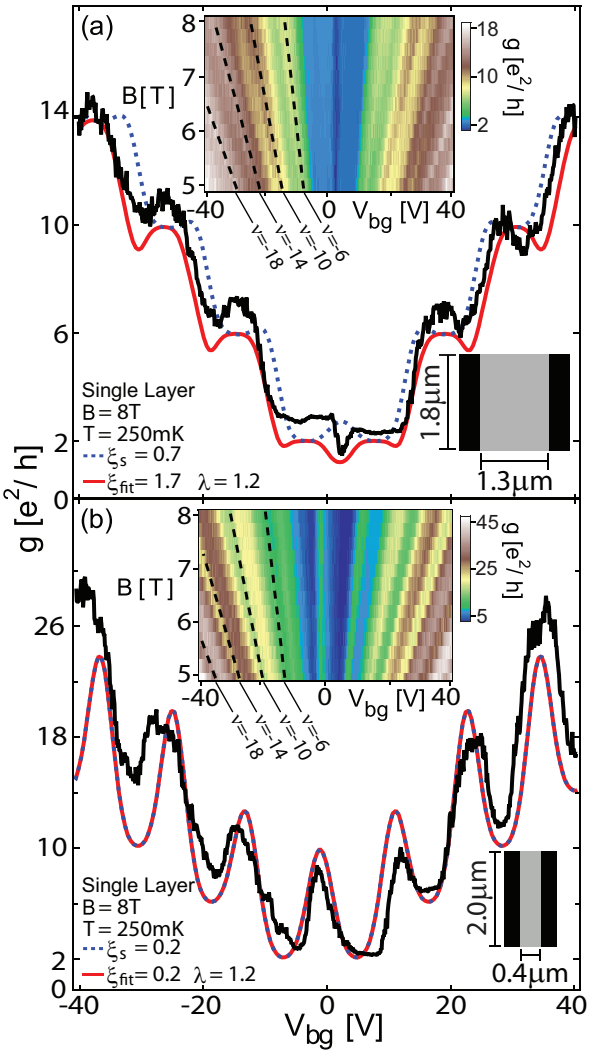

FIG. 2: (color online) (a) Inset: Conductance g in the quantum Hall regime as a function of B and $V_{\rm bg}$ at T = 250 mK for sample A1. Black dashed lines correspond to filling factors of $\nu = -6, -10, -14, -18$ and align with the local *maxima* of conductance. Main: (black) Horizontal cut of inset giving $g(V_{\rm bg})$ at $B = 8\,{\rm T}$ and calculated g for the best-fit equivalent aspect ratio $\xi_{\rm fit} = 1.7$ (solid red curve) and the actual sample aspect ratio $\xi_s = 0.7$ (dashed blue curve) using Landau level broadening parameter $\lambda = 1.2$. (b) Inset: Conductance g in the quantum Hall regime as a function of B and $V_{\rm bg}$ at T = 250 mK for sample A2. Black dashed lines correspond to filling factors of $\nu = -6, -10, -14, -18$ and align with the local *minima* of conductance. Main: (black) Horizontal cut of inset giving $g(V_{\rm bg})$ at $B = 8\,{\rm T}$ and calculated g for $\xi_{\rm fit} = 0.2$ (solid red curve) and $\xi_s = 0.2$ (dashed blue curve) ($\lambda = 1.2$, the same as sample A1).

aspect ratio $\xi_{\rm fit} = 0.2$ agrees well with the measured ξ_s for sample A2.

We observe that the size of peaks and dips in Fig. 2(a,b) increases for higher LL. In contrast, theory[11] predicts that peaks and dips at $|\nu| > 0$ LLs are all roughly the same. This discrepancy may reflect the inapplicability of the two-phase model approach of Ref. [19], which underlies the semicircle law obtained in this work, to

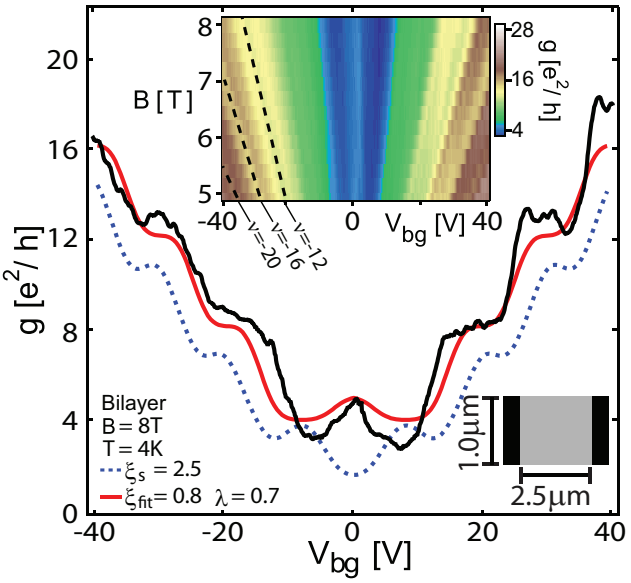

FIG. 3: (color online) Inset: Measured g of sample B1 as a function of B and $V_{\rm bg}$ at $T = 4$K. Black dashed lines, corresponding to $\nu = -12, -16, -20$, align with local *minima* of g. No minima are observed at $\nu = 8$ for $5\text{T} < B < 8\text{T}$. Main: Horizontal cut of inset at $B = 8$T (black), and calculated g using $\lambda = 0.7$ for $\xi_s = 2.5$ (dashed blue curve) and $\xi_{\rm fit} = 0.8$ (solid red curve).

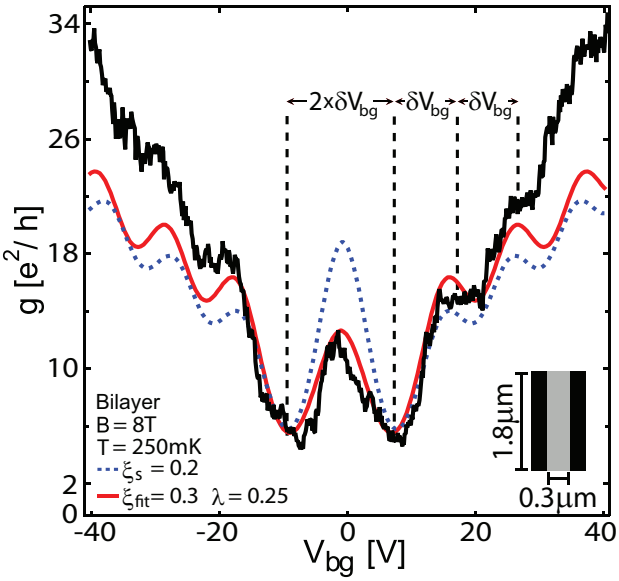

FIG. 4: (color online) Measured $g(V_{\rm bg})$ for sample B2 (black) and the calculated g using $\lambda = 0.25$ for $\xi_s = 0.2$ (dashed blue trace) and $\xi_{\rm fit} = 0.3$ (solid red trace). Two key features in the curve suggest this sample is a gapless bilayer, namely, a pronounced peak in g near the CNP, and the larger spacing between the two minima straddling the CNP compared to the spacing $\delta V_{\rm bg} \sim 9.5$ between other consecutive minima.

higher LLs. Indeed, because for Dirac particles the spacing between LLs decreases at higher energies as an inverse square root of the level number, one may expect mixing between non-nearest LLs to increase at high energies. Such mixing can lead to the longitudinal conductivity values in excess of those of Ref. [19], which only considers mixing between nearest LLs (see the discussion in Ref. [20]).

To take these effects into account, we extend the model of Ref. [11] by assuming that the contribution of the $n^{\rm th}$ LL to the conductivity tensor in monolayer graphene is described by a modified semicircle ("elliptic") law,

$$\delta_n\sigma_{xx}^2 + A_n^2(\delta_n\sigma_{xy} - \sigma_{xy,n}^0)(\delta_n\sigma_{xy} - \sigma_{xy,n'}^0) = 0, \quad (1)$$

where $\delta_n\sigma_{xx}$ and $\delta_n\sigma_{xy}$ are the effective longitudinal and Hall conductivities, $\sigma_{xy,n}^0$ and $\sigma_{xy,n'}^0$ are the quantized Hall conductivities at the neighboring plateaus. Here n and n' are neighboring LL indices, related by $n' = n + 1$ (except the doubly degenerate $\nu = 0$ LL for the bilayer, in which case $n = -1$ and $n' = 1$). The A_n account for departures from the semicircle law. We take $A_n \approx 1$ for $n = 0, \pm 1$, and $A_n \approx 2$ for other LLs, consistent with previous observations.[20]

III. BILAYER SAMPLES

The black curve in Fig. 3 shows measured $g(V_{\rm bg})$ for sample B1 ($\xi_s = 2.5$) at $B = 8$T and $T = 4$K. This sample has two features indicating that it is a bilayer sample: plateaus in conductance appearing near 4, 8, 12 and $16\,e^2/h$, and a conductance maximum at the CNP whose relative size is much larger then those at higher LLs. The conductance values at the plateaus $\nu = \pm 4$ here are lower than the expected $4\,e^2/h$ for a bilayer sample, falling to $2.7(3.1)\,e^2/h$ on the electron (hole) side of the CNP. The peak value in conductance at $\nu = 0$ ($V_{\rm bg} = 0.5\,\text{V}$) is $5\,e^2/h$. At higher filling factors, the plateaus exhibit two different behaviors, showing a flat plateau at $\nu = 8$ and a plateau followed by a dip at $\nu = 12$. The small dips align with the filling factors $\nu = -12, -16, -20$ for $5\,\text{T} < B < 8\,\text{T}$ (see inset of Fig. 3), using $\alpha = 7.2 \times 10^{10}\text{cm}^{-2}\text{V}^{-1}$ and $V_{\rm offset} = 0.5$V.

Theoretical g curves for aspect ratios $\xi_s = 2.5$ (dashed blue curve) and $\xi_{\rm fit} = 0.8$ (solid red curve) are shown in Fig. 3. Theoretical $g(V_{\rm bg})$ curves for these two aspect ratios are similar at high density, but differ for $\nu = 0$: the curve for $\xi_s = 2.5$ has a dip in conductance at the CNP while the best-fit curve ($\xi_{\rm fit} = 0.8$) has a peak, similar to the experimental curve. The curve for $\xi_{\rm fit} = 0.8$ also agrees better with experiment at higher densities.

In some cases the quantized conductance values are found to be quite different from the expected quantized values, as demonstrated in Fig. 4 for sample B2 ($\xi_s = 0.2$). In this sample, g reaches a maximum of $13.5\,e^2/h$ at the CNP, with adjacent minima of $5\,e^2/h$. Away from the CNP, conductance plateaus appear at values of $\sim 16\,e^2/h$ and $23\,e^2/h$, neither of which are near expected values for monolayer or bilayer graphene. Since there are no strong peaks or dips in g away from charge neutrality, as is expected for a device with a $\xi_s \ll 1$, it is difficult to determine the number of layers from the loca-

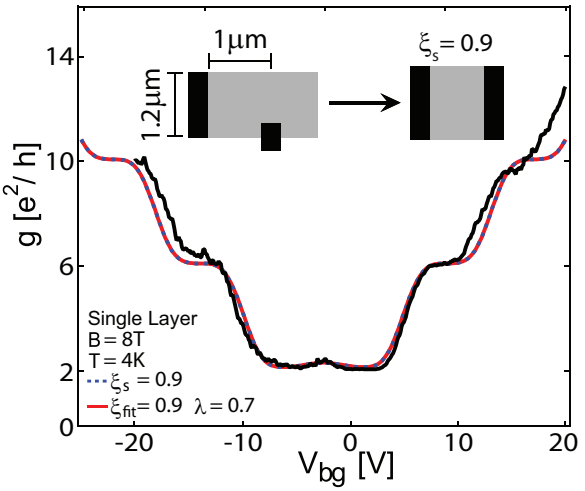

FIG. 5: (color online) Measured $g(V_{\rm bg})$ for sample C (black) and calculated conductance (solid red curve) for $\xi_{\rm fit} = 0.9$ ($\lambda = 0.7$). The asymmetric contacts of this sample can be conformally mapped onto a rectangle, producing a device aspect ratio of $\xi_s = 0.9$ (dashed red curve, directly under solid red curve).

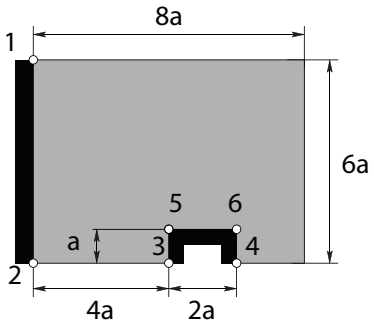

FIG. 6: (color online) A polygon representing sample C (see Fig. 5). Black regions correspond to contacts, length scale $a = 200\,$nm.

tion of the conductance extrema. There are two conductance features, however, that suggest the sample is gapless bilayer graphene. First, the peak at $\nu = 0$ is much more pronounced than any other peak in the conductance. Second, the spacing in $V_{\rm bg}$ between the two lowest LLs is twice as large as the spacing between any other two successive LLs (in Fig. 4, $\delta V_{\rm bg} \sim 9.5\,$V). Both features arise in bilayers as a result of the zero-energy LL being eightfold degenerate, twice as much as all other bilayer LLs and the zero-energy LL in single layer graphene.[6] The theoretical prediction, using $\xi_{\rm fit} = 0.3$ (solid red line) and $\xi_s = 0.2$ (dashed blue line), for the bilayer sample B2 are shown in Fig. 4.

IV. NON-RECTANGULAR SAMPLES

In this section we extend the comparison of theory and experiment to a non-rectangular device, sample C, shown schematically in the inset of Fig. 5. The measured two-terminal conductance of sample C (black curve in Fig. 5) has properties very similar to those expected for a square monolayer sample: around the CNP the conductance is nearly flat with value close to $2\,e^2/h$, monotonically increasing on the electron and hole sides at filling factors $|\nu| > 2$.

Theoretical curve shown in Fig. 5 is obtained from the conducting rectangle model using a best-fit effective aspect ratio $\xi_{\rm fit} = 0.9$ and the LL broadening parameter $\lambda = 0.7$. This choice of parameters yields particularly good agreement for $|\nu| \leq 6$. At higher fillings, the plateaus are washed out, suggesting that the LL broadening is stronger for LLs $|n| \geq 2$. It is interesting to compare the best-fit value $\xi_{\rm fit}$ to an effective aspect ratio, obtained from conformal mapping of sample C to a rectangle. As discussed below, this conformal mapping can be constructed directly, owing to the relatively simple geometry of sample C. The effective aspect ratio obtained in this way is $\xi_s \approx 0.9$, which is consistent with the best-fit value.

Before we proceed to construct the conformal mapping we note that the geometry of sample C, pictured in Fig. 6, is that of a polygon. In principle, any polygon can be mapped onto the upper half-plane by inverting a Schwarz-Christoffel mapping.[21] However, since this mapping is defined by a contour integral, the inverse mapping can only be found numerically. In order to circumvent this difficulty, two approximations are employed below, allowing the desired mapping to be constructed as a composition of a few simple mappings.

The steps involved in this construction are illustrated in Fig. 7. First, the rectangular shape in Fig. 6 is replaced by a semi-infinite strip shown in Fig. 7(a). This approximation should not significantly affect the conductance, as the current flows mostly in the region between contacts 1-2 and 3-4. Without loss of generality we set the length scale $a = 1$.

Our next step is to straighten out the contact 3-5-6-4. For that, let us consider an auxiliary mapping that maps the upper $\tilde{w}$ plane onto the upper $\tilde{z}$ plane with a removed rectangle[22]:

$$\tilde{z} - iA = \int_0^{\tilde{w}} \left(\frac{\xi^2 - 1}{\xi^2 - 2}\right)^{1/2} d\xi. \qquad (2)$$

We choose the parameter A to be equal

$$A = \int_0^1 \left(\frac{\xi^2 - 1}{\xi^2 - 2}\right)^{1/2} d\xi \approx 0.60, \qquad (3)$$

so that the removed rectangle has vertices

$$\tilde{z}_{3,4} = \pm A, \;\; \tilde{z}_{5,6} = \pm A + iA. \qquad (4)$$

These points correspond to the points $\tilde{w}_{3,4} = \pm\sqrt{2}$, $\tilde{w}_{5,6} = \pm 1$ in the $\tilde{w}$ plane. The value of A ensures that the edge of the sample on the x axis remains on the x axis under the mapping (2). The distance between points

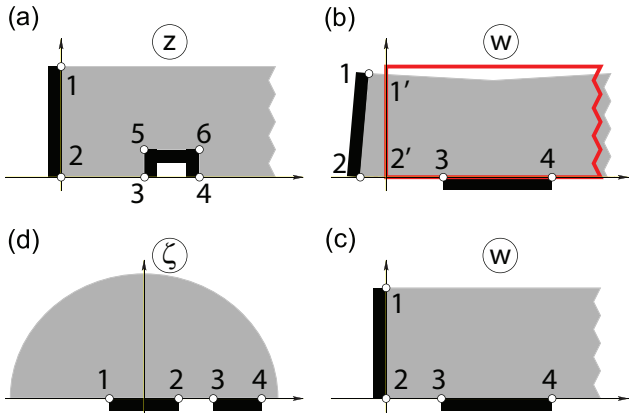

FIG. 7: (color online) Three steps used to map the polygon in Fig. 6 (sample C) onto the upper half-plane (schematic). First, the rectangle in Fig. 6 is replaced by a half-infinite strip, extending indefinitely to the right (a). Next, we map the domain shown in (a) onto a rectangle with contact 3-5-6-4 straightened out (b). Under this mapping, the sample is slightly distorted, as indicated by the grey polygon in (b). Because the deviation of the grey polygon boundary from the original sample boundary (red line in (b)) is fairly small, it can be neglected, giving a half-infinite strip (c). Finally, the domain (c) is mapped onto the upper half-plane (d), which allows to find the cross ratio Δ_{1234}, Eq. (9), and evaluate the effective aspect ratio, Eq. (10).

$\tilde{z}_3$ and $\tilde{z}_5$ plane equals A, as follows from Eq. (2) and the identity

$$\int_1^{\sqrt{2}} \left|\frac{\xi^2-1}{\xi^2-2}\right|^{1/2} d\xi = \int_0^1 \left(\frac{\xi^2-1}{\xi^2-2}\right)^{1/2} d\xi, \qquad (5)$$

which can be proved by making the change of variables, $\xi = \sqrt{2-x}$ in the integral in the left-hand side of Eq. (5), and $\xi = \sqrt{x}$ in the integral in the right-hand side of Eq. (5).

The removed rectangle has aspect ratio equal to 2, the same as that for the contact 3-5-6-4, however, their dimensions differ by a factor of A. Scaling and shifting both $\tilde{z}$ in $\tilde{w}$,

$$\tilde{z} = A(z-5), \;\; \tilde{w} = A(w-5), \qquad (6)$$

we obtain the required mapping which straightens out the contact 3-5-6-4.

The second approximation is necessary because the mapping (2), (6), while straightening the segments 3-5-6-4, distorts the rest of the boundary. We notice, however, that sufficiently far from the contact 3-5-6-4 the mapping (2) is close to the identity:

$$z(w \gg 1) = w + O(1/w), \quad |z-5| \gg 1. \qquad (7)$$

This property and the relatively small size of the segments 3-5-6-4 compared to the strip width guarantees that the distortion is small. This is shown schematically in Fig. 7(b), where the curved grey polygon represents the actual image of the sample, with the deviation of its boundary from the strip of the same asymptotic width (shown in red and exaggerated for clarity). The deviation is indeed small: by investigating the mapping (2), (6) numerically we found that the boundary is displaced the most at the point 2 which is shifted by approximately 0.3 away from its original position $2'$ along the real axis. This is small compared to the sample width, equal to 6, which allows us to neglect the displacement of the boundary. Thus we assume that the mapping (2), (6) transforms sample C into the semi-infinite strip shown in Fig. 7(c).

After this approximation is made, it is straightforward to transform the semi-infinite strip in Fig. 7(c) into the upper half-plane, which can be done by the following mapping,

$$\zeta = \cosh\frac{\pi w}{6}. \qquad (8)$$

In the ζ plane, the contacts are mapped on the real axis, with the end points 1, 2, 3 and 4 mapped to $\zeta_1 = -1$, $\zeta_2 = 1$, $\zeta_3 \approx 2.11$, $\zeta_4 \approx 23.57$. From these values, following the procedure described in Ref. [11] (Appendix), we compute the cross ratio

$$\Delta_{1234} = \frac{(\zeta_1-\zeta_4)(\zeta_3-\zeta_2)}{(\zeta_1-\zeta_2)(\zeta_3-\zeta_4)} \approx -0.64, \qquad (9)$$

and then obtain the aspect ratio from the relations

$$\xi_s = \frac{L}{W} = \frac{K(k')}{2K(k)}; \quad \Delta_{1234} = (1-k^2)/2k, \qquad (10)$$

where $K(k)$ is the complete elliptic integral of the first kind, and $k' = (1-k^2)^{1/2}$. This procedure yields the value $\xi_s = 0.9$, identical to that found from the best fit to a conducting rectangle model (see Fig. 5).

V. SUMMARY AND DISCUSSION

In summary, we have studied the effect of geometry on the conductance of two-terminal graphene devices in the QH regime, comparing experiment and theory. The quantized QH plateaus typically exhibit conductance extrema that are stronger for wide, short samples. For non-rectangular samples, the equivalent rectangle approach appears works well.

Theoretically, for short, wide samples ($\xi_{\rm fit} < 1$) the two-terminal conductance a conductance minimum is expected at filling factors where plateaus exist in multiterminal devices, while for long, narrow samples ($\xi_{\rm fit} > 1$), a conductance maximum is expected at these filling factors. Along with the behavior at the CNP, these signatures provide a clear way to identify the number of layers in the sample even when the quantization is weak or absent.

We find in the five samples measured that conductance as a function of gate voltage is well described by theory, allowing for a phenomenological Landau Level broadening, and treating the aspect ratio as a fit parameter. In

some samples, however, the best fit aspect ratio differs considerably from the measured aspect ratio of the sample.

What might lead to the discrepancy between some of the measured and fit aspect ratios? One source of discrepancy could be that only part of the contact actually injects current. It might also be that the contacts locally dope the graphene, causing the aspect ratio to appear smaller. This latter scenario, however, would require that the doping penetrates $\sim 500\,\mathrm{nm}$ into the graphene, which is ~ 2 orders of magnitude larger than expected.[23] Another, more interesting possibility could be that the picture of an effective medium characterized by local conduction, on which the argument leading up to the semi-circle relation[19] is based, may not hold. This might arise, for instance, from large density fluctuations, giving rise to electron and hole puddles[24] forming a network of p-n interfaces along which conduction occurs. In this case, the effect of the back gate is to alter the percolation properties of this p-n network. Transport mediated by such states would almost certainly change the conventional picture of local conduction. Further studies are required to clarify the physical mechanism responsible for the observed behavior.

Acknowledgement. Research supported in part by INDEX, an NRI Center, the Harvard NSEC, and the Harvard Center for Nanoscale Systems (CNS), a member of the National Nanotechnology Infrastructure Network (NNIN), which is supported by the National Science Foundation under NSF award no. ECS-0335765. We thank Pablo Jarillo-Herrero for helpful discussions.

---

* Present address: Department of Applied Physics, Yale University, New Haven, Connecticut 06520, USA

[1] K. S. Novoselov *et al.*, Nature **438**, 197 (2005).
[2] Y. Zhang *et al.*, Nature **438**, 201 (2005).
[3] K. S. Novoselov *et al.*, Nat. Phys. **2**, 177 (2006).
[4] A. K. Geim and K. S. Novoselov, Nat. Mater. **6**, 183 (2007).
[5] V. P. Gusynin and S. G. Sharapov, Phys. Rev. Lett. **95**, 146801 (2005).
[6] E. McCann and V. I. Falko, Phys. Rev. Lett. **96**, 086805 (2006).
[7] H. B. Heersche *et al.*, *Nature* **446**, 56 (2007).
[8] J. R. Williams, L. DiCarlo and C. M. Marcus, Science **317**, 638 (2007).
[9] B. Özyilmaz *et al.*, Phys. Rev. Lett. **99**, 166804 (2007).
[10] C. W. J. Beenakker and H. van Houten, *Solid State Physics*, edited by H. Ehrenreich and D. Turnbull (Academic, New York, 1991), Vol. 44, pg. 1.
[11] D. A. Abanin and L. S. Levitov, Phys. Rev. B **78**, 035416 (2008).
[12] E. McCann, Phys. Rev. B **74**, 161403(R) (2006).
[13] E. V. Castro *et al.*, Phys. Rev. Lett. **99**, 216802 (2007).
[14] J. B. Oostinga *et al.*, Nat. Mater. **7**, 151 (2007).
[15] R. F. Wick, J. Appl. Phys. **25**, 741 (1954).
[16] H. H. Jensen and H. Smith, J. Phys. C **5**, 2867 (1972).
[17] R. W. Rendell and S. M. Girvin, Phys. Rev. B **23**, 6610 (1981).
[18] K. S. Novoselov *et al.*, Science **306**, 666 (2004).
[19] A. M. Dykhne and I. M. Ruzin, Phys. Rev. B **50**, 2369 (1994).
[20] C. P. Burgess and B. P. Dolan, Phys. Rev. B **76**, 113406 (2007).
[21] T. A. Driscoll and L. N. Trefethen, *Schwarz-Christoffel Mapping*, (Cambridge University Press, Cambridge, 2002).
[22] Online Conformal Mapping dictionary, example 51: http://math.fullerton.edu/mathews/c2003/ConformalMapDictionary.5.html
[23] G. Giovannetti *et al.*, Phys. Rev. Lett. **101**, 026803 (2008).
[24] J. Martin *et al.*, Nat. Phys. **4**, 144 (2008).